Probing Amyloid Aggregation and Morphology *In Situ* by Multiparameter Imaging and Super-Resolution Fluorescence Microscopy

Gabriele S. Kaminski Schierle

Department of Chemical Engineering and Biotechnology, University of Cambridge, Cambridge, United Kingdom

Markus Sauer

Department of Biotechnology and Biophysics, Julius-Maximilians-University Würzburg, Würzburg, Germany

Clemens F. Kaminski

Department of Chemical Engineering and Biotechnology, University of Cambridge, Cambridge, United Kingdom

Chapter Outline

INTRODUCTION

The phenomenon of protein misfolding and aggregation is one of the most important topics in current biomedical research [1]. The failure of proteins to fold correctly, or to remain correctly folded, lies at the center of a growing number of increasingly prevalent pathologic conditions, referred to collectively as misfolding disorders, that range from Parkinson's and Alzheimer's diseases to type II diabetes, and cystic fibrosis [1]. One of the most common pathogenic consequences of protein misfolding is the formation of aggregates that result in the deposition of the protein concerned as amyloid fibrils and plaques [2]. These species are associated with the prevalent forms of neurodegenerative disorders, particularly those associated with aging, and therefore an understanding of their formation and behavior *in situ* in biologic systems is of paramount importance [1,3]. Another key requirement in developing such an understanding lies in an ability to observe directly the nature and kinetics of the aggregation process *in vivo*. These objectives have, however, proved to be extremely challenging to achieve and indeed the physiologic roles of the variety of misfolded species formed during the process of aggregation in biologic systems are not yet understood in any detail [4]. Traditional

imaging techniques, such as transmission electron microscopy (TEM) and atomic force microscopy (AFM), are powerful methods [1], but require elaborate sample preparation protocols, are difficult to be applied dynamically over extended periods of time, and their invasive nature makes them unsuitable for observations within living organisms. Optical techniques do not suffer from such limitations and permit the non-invasive visualization of amyloidogenis *in situ*, and even *in vivo* [5–10].

In this chapter we focus on two powerful new methods to quantify protein aggregation reactions in biologic systems. We show how changes in parameters such as the polarization state of reporter molecules and fluorescence lifetime offer sensitive information on the amyloid aggregation state in techniques we collectively refer to as *multiparameter microscopy* [11–13], reviewed below. We show that these techniques are powerful – particularly for applications in live-cell and organism models of aggregation diseases. The second technique, *direct* stochastic optical reconstruction microscopy, *d*STORM, offers direct information on the shape and size of protein fibrils *in situ* in cells, at a resolution approaching that of electron microscopy techniques. It is reviewed later in this chapter in a section headed *Super-resolution imaging of amyloid aggregation*; this begins with an outline of the method in theory and practice before examples are given of its application in the study of amyloidogenesis.

MULTI-PARAMETER MICROSCOPY OF PROTEIN AGGREGATION KINETICS

### Fusion Protein Labeling of Amyloidogenic Proteins

For microscopy in live cells or organisms, fluorescent proteins (FP) are indispensable. Various FP model systems for protein aggregation have been developed, including the nematode worm *Caenorhabditis elegans (C. elegans)*, the fruit fly *Drosophila melanogaster*, and even mice. FP tagging has been used in animal models to study the misfolding

and accumulation of α-synuclein (AS) [14–17], a protein involved in Parkinson's disease, and other proteins associated with various misfolding diseases [18–22].

The conjugation of relatively bulky FPs (~28 kDa) to amyloid proteins may, however, perturb the native structure of the latter and interfere with folding and aggregation properties. In the case of small, structurally unfolded proteins such as, e.g. AS (~14 kDa), this appears to be of particular concern. Not surprisingly, some controversy has arisen regarding studies of AS misfolding and aggregation with FPs *in vivo*, and rigorous validation of such model systems by biophysical techniques is essential. In Van Ham et al [23] we presented a detailed biophysical characterization of the properties of AS tagged on its C-terminal with the yellow fluorescent protein (YFP) variant Venus. The resulting fusion protein, AS-YFP, was appraised for its merit as a reporter of AS misfolding and aggregation.

The construct was produced by fusing Venus to the C-terminus of AS, separated by a short linker peptide designed to minimize steric interference effects on folding of the polypeptide chain [21]. We compared the aggregation behavior of AS-YFP with that of wild-type AS *in vitro* and both moieties exhibited increasing ThT fluorescence in time and displayed similar kinetics of amyloid formation (Fig. 10.1A).

The structure of the amyloid deposits of AS-YFP were further analyzed by TEM. Both width and length of individual fibrils showed no significant differences between wild-type AS and AS-YFP (Fig. 10.1B). Furthermore, we performed NMR studies and a comparison of the normalized intensities of $^1H–^{15}N$ cross peaks to assess structural difference in the obtained aggregates. The method is sensitive to conformational dynamics of AS and interactions with the solvent [24–26] and revealed that YFP-mediated perturbations were subtle and confined to the C-terminal region of the protein, around residues 120 to 140 (Fig. 10.1C). Hence, we conclude that structural and dynamical perturbations are minor to the overall folding characteristics of the peptide chain and restricted to the local region to which the YFP has been attached.

(A) **(B)** AS   AS-YFP   **(C)**
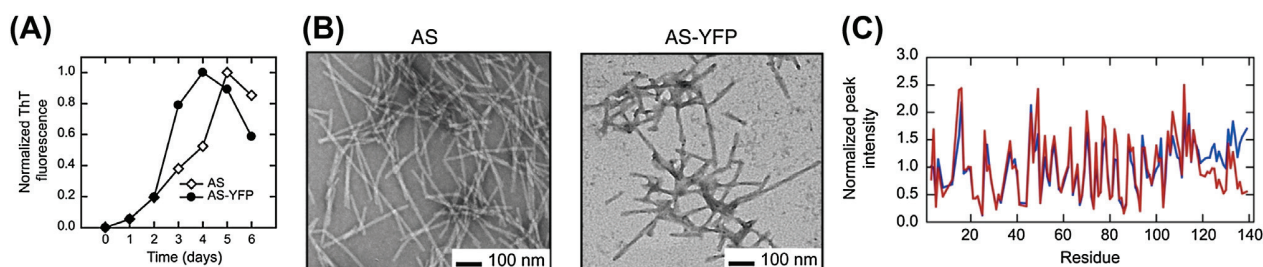
FIGURE 10.1   Both wt α-synuclein (AS) and AS-YFP form amyloid structures as shown *in vitro*. (A) Normalized ThT fluorescence of wt AS (open diamonds) and of AS-YFP (filled circles). (B) High magnification TEM images of wt AS and AS-YFP fibrils displaying similar morphologies. (C) Normalized $^1H–^{15}N$ HSQC peak intensities for wt AS (blue) and AS-YFP (red). Peak intensities only differ between residues 120 and 140. With permission from reference 23.

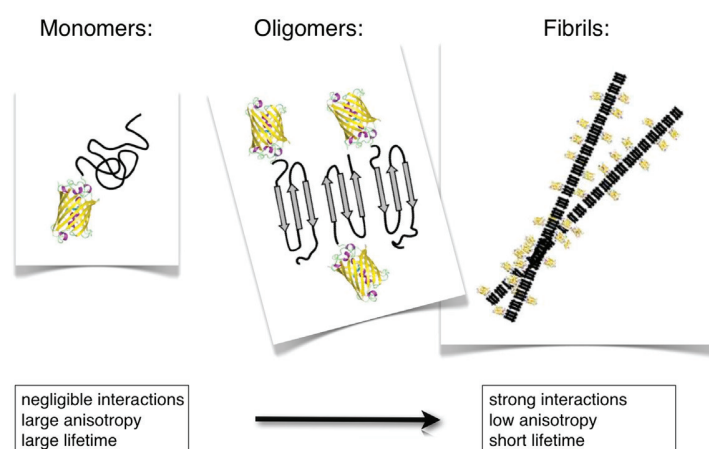## Principle of Multi-Parameter Imaging Techniques

Figure 10.2 shows the principle of multi-parameter imaging methods [11,12,27,28] for investigating protein aggregation. Because the spectral properties of reporter fluorophores are affected by changes in their local environment, increasing degrees of oligomerization lead to changes in spectrum, lifetime and polarization state of the fluorophore, which are mediated by a variety of biophysical interactions. Examples are non-resonant energy transfer between the reporter fluorophores (homoFRET), leading to changes in the polarization state of the emitted light; fluorescence quenching, reflecting changes in the environment in which the fluorophore is embedded, leading to changes in the fluorescence lifetime; etc. We review homoFRET and lifetime changes in more detail in the following sections as they are particularly powerful methods for probing the amyloid aggregation state in biologic systems.

Fluorescence Anisotropy Imaging

Principle of HomoFRET in the Study of Protein Self-Assembly Reactions

Förster resonance energy transfer (FRET) is an electrostatic dipole–dipole interaction between molecules in close proximity in which energy from an initially excited donor molecule is transferred, non-radiatively, to an acceptor molecule [29–31]. In so-called heteroFRET this process takes place between spectrally distinct donors and acceptors. FRET between like molecules, termed homoFRET, is also possible and occurs for fluorophores exhibiting small Stokes shifts, such that their excitation spectrum partially overlaps with their own emission spectrum (see Fig. 10.3). On aggregation, the proximity between fluorophores decreases, and

the level of homoFRET increases providing a readout for the aggregation state. In contrast to heteroFRET, however, homoFRET cannot be quantified via intensity, spectral or lifetime changes because donor and acceptor molecules are of the same moiety and hence spectroscopically indistinguishable [32]. HomoFRET can, however, be detected via changes in the polarization state of the emitted fluorescence, as argued in the following. Upon aggregation, the average distance between fluorphores decreases and homoFRET becomes appreciable at inter-fluorophore distances below the Förster radius R_0, which is of the order of 3–5 nm for typical FPs. Because the molecules participating in homoFRET have a distribution of dipole orientations, fluorescence emitted from sensitized acceptor molecules will be more depolarized than their non-sensitized counterparts. This presents an opportunity for cluster size quantification through a measurement of the degree of fluorescence anisotropy loss (degree of polarization loss), when polarized input light is incident on the sample: aggregation increases homoFRET, and, hence, leads to a significant loss in polarization anisotropy. The maximum amount of homoFRET depolarization for a defined cluster occurs when the energy transfer has reached equilibrium, that is, a point where all molecules in the cluster have an equal probability of emitting a photon, indicative of numerous electrostatic interactions between the participating molecules. Thus, the larger the number of molecules in a cluster, the lower the anisotropy of the overall fluorescence becomes due to increasing contributions from sensitized acceptor emission. This is illustrated in Figure 10.3C. Note that, in addition to sensitized emission via homoFRET, rotational diffusion of fluorophores can also lead to fluorescence depolarization, but for typical rotational correlation times of bulky fusion proteins in aqueous environments ($\Phi{\sim}20$ ns) this contribution is negligible compared to homoFRET. It must be stated

Monomers: Oligomers: Fibrils:

negligible interactions
large anisotropy
large lifetime

strong interactions
low anisotropy
short lifetime

FIGURE 10.2   Principle of multiparametric fluorescence imaging of protein aggregation kinetics. Labeled monomers aggregate into fibrillar structures, bringing fluorophores within interaction distances, and leading to polarization losses (via homoFRET). Furthermore, the changing molecular environment upon amyloidogenesis leads to structure-specific lifetime changes in the aggregating species.
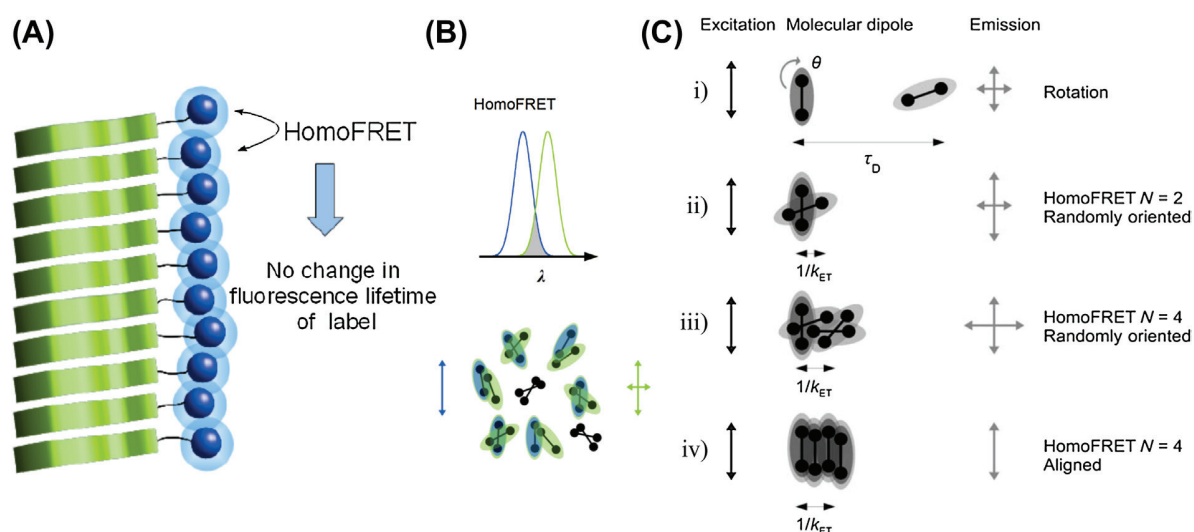
FIGURE 10.3   (A) HomoFRET sensor reports on aggregation but is independent of fluorescence lifetime changes. (B) *Top image*. HomoFRET results from overlap between the absorption (blue) and emission (green) spectra of a single type of fluorophores. *Bottom image*. When homoFRET occurs in dimers, the emitted fluorescence consists of direct donor emission and sensitized acceptor emission. The fluorescence is thus not completely depolarized. (C) Fluorophores excited by linearly polarized light emit depolarized fluorescence due to rotational diffusion and/or homoFRET. (i) A fluorophore with rotational correlation time θ shorter than its fluorescence lifetime τ_D emits fluorescence with polarization orientation unaligned with that of the excitation light. (ii, iii) HomoFRET between randomly-oriented fluorophores in clusters leads to depolarized emission – bigger clusters lead to more depolarized fluorescence emission. (iv) However, if molecular dipoles of the fluorophores in a cluster are aligned with each other, little depolarization will occur. HomoFRET occurs on a shorter timescale than rotational diffusion (t≈$1/k_{ET}$ for FRET and θ for rotational diffusion), allowing experimental identification by time-resolved anisotropy measurements. With permission from reference 32.

that relative anisotropy changes become smaller as cluster size increases, making the technique more useful for quantifying smaller clusters, i.e. it is most sensitive for probing the onset of aggregation [32].

HomoFRET Imaging for the Study of α-synuclein Aggregation

HomoFRET anisotropy imaging was used for studying amyloid aggregates of AS *in vitro* as a model of Parkinson's disease (Fig. 10.4) [23]. The example shows that, upon aggregation, the high anisotropy for soluble monomeric proteins decreases due to homoFRET among the attached YFP-labels. The anisotropy decreases monotonically as a function of aggregation time but the observed changes cannot be uniquely related to changes in oligomer size because they are not only a reflection of aggregate size but also of the relative fraction of monomeric versus aggregated species in the measurement volume. The method has great potential to screen for anti-aggregating drugs and to test their efficacy. Because fusion proteins are used, the technique can furthermore be used in live cells. HomoFRET is a very sensitive method for detecting the onset of protein aggregation and is straightforward to use. In a wide-field-imaging set-up [33,34] the technique permits drug screens to be parallelized efficiently both *in vitro* and in live-cell models of aggregation. However, a drawback is the limited sensitivity of the technique with growing cluster size, limiting its dynamic range. For cluster

sizes >5 the fluorescence emission becomes essentially fully depolarized and no further changes are therefore expected on continued aggregation.
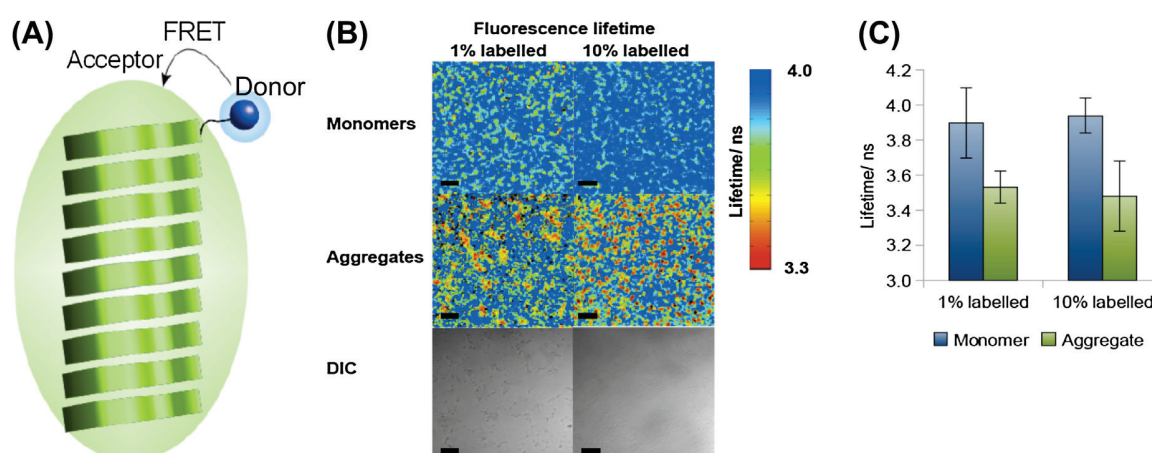
Fluorescence Lifetime Imaging of Protein Aggregation

The Fluorescence Lifetime of Peptide Labels Reports on Amyloid Aggregation

During our studies on homoFRET of aggregating proteins we noticed that increasing aggregation of AS-YFP was accompanied by large reductions in the YFP fluorescence lifetime, which correlated with increasing degrees of aggregation. This finding was unexpected because the homoFRET process does not lead to lifetime changes in participating fluorphores (see earlier discussion). This finding led to our discovery that amyloidogenesis is accompanied by the emergence of intrinsic energy states in growing amyloid fibrils (see Chapter 13 in this book). We associate this with extensive hydrogen bonding networks which develop in the emerging cross-β-sheet scaffolds that run in regular patterns along the entire fibril axis. These energy states are also linked to an intrinsic fluorescence phenomenon occurring upon amyloid fibrillogenesis that has been observed by us [9,35,36] and also by other workers [37–39]. The intrinsic energy states are capable of absorbing energy in the visible range and thus offer excellent potential for a novel sensor concept based on energy
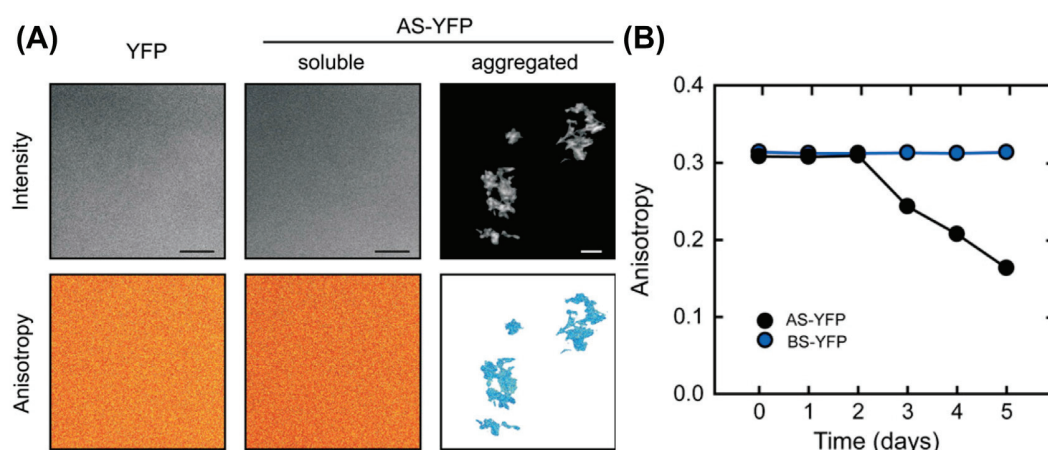
FIGURE 10.4   FAIM images of YFP-labeled α-synuclein aggregates *in vitro*. HomoFRET among YFP-labels on aggregated recombinant AS leads to depolarized fluorescence. (A) Fluorescence intensity (top row) and anisotropy (bottom row) images of AS-YFP in soluble and aggregated form (columns 2 and 3). Column 1 shows a control experiment for purified YFP in solution. (B) Spatially averaged anisotropy as a function of time for AS-YFP (shown in black) and β-synuclein-YFP (BS-YFP), a moiety which does not aggregate. For BS-YFP, no anisotropy changes are observed in time. Scale bars represent 5 μm. With permission from reference 23.

FIGURE 10.5   (A) HeteroFRET sensor reports on aggregation with an improved dynamic range and requires low labeling densities. (B) Fluorescence lifetime images of 10 μM K18 Tau plus 2.5 μM heparin in 50 mM ammonium acetate at pH 7.4 and 37°C. Images correspond to K18 Tau labeled with Alexa-488 at C260 at 1% monomer labeling fraction (left column) and 10% monomer concentration (right column) respectively (C). On aggregation, Alexa-488 indicates a similar decrease in fluorescence lifetime for both samples to 3.5 ns from the initial lifetime of the monomers of 3.9 ns. The lifetime is thus not significantly dependent on the fluorophore labeling fraction (see histograms). It should be noted that concentrations of dyes are below what is required for homoFRET to occur, hence excluding fluorophore–fluorophore interactions for the lifetime effect. Scale bars represent 30 μm.

transfer from a fluorophore label to the emerging β-sheet scaffold of the amyloid protein. The interaction between the amyloid scaffold and the fluorophore is directly correlated with the extent of amyloid formation by the peptide chain, and can be conveniently quantified *via* changes in the fluorescence lifetime of the extrinsic fluorophore label [9]. The lifetime of the attached fluorophore decreases in proportion to the degree of amyloid aggregation and is insensitive to fluorophore concentration and hence labeling stoichiometries (i.e. label-to-peptide ratios) much smaller than one suffice. This offers an exciting advantage compared to homoFRET, which requires very dense labeling of the amyloid structure. Sparse labeling is less likely to generate perturbations

to the aggregation process, an issue that may bear particular relevance in the highly crowded molecular environments prevailing *in vivo*. We tested these attributes quantitatively using mixtures of fluorescently labeled and unlabeled monomers of an aggregation-prone variant of human Tau protein (K18 Tau), a key species involved in Alzheimer's disease. The labeled and unlabeled peptides were mixed at relative concentrations of 1:100, and 1:10, respectively (Fig. 10.5), concentrations too low for homoFRET to take place [23]. In the experiment, Alexa Fluor 488 maleimide was covalently linked to the cysteine residue at position 260 of K18 Tau to act as donor fluorophore in the sensor. Figure 10.5B shows the resulting fluorescence lifetime images for a period

of 4 hours of incubation, while Figure 10.5C shows corresponding plots of the fluorescence lifetimes of the Alexa Fluor 488 labels in the aggregates. Both label stoichiometries lead to near identical lifetime changes upon aggregation, verifying the concentration independence of the sensor concept.

In Vivo FLIM Imaging of Protein Aggregation

The power of the sensor concept was demonstrated in an aggregation model of AS-YFP in the nematode worm

Caenorhabditis elegans. Images of the whole anterior regions of intact *C. elegans* were taken at various time points during the lifespan of AS–YFP transgenic worms, and the average fluorescence lifetime determined in each case. Over a period of 15 days the fluorescence lifetime of AS–YFP decreases (by ~130 ps) as aggregates appear in the animal (Fig. 10.6A, second image in panel, and Fig. 10.6B, black bars). The techniques permit for the first time the kinetic imaging of amyloid aggregation in a multicellular living organism. Importantly, no reductions in lifetime were
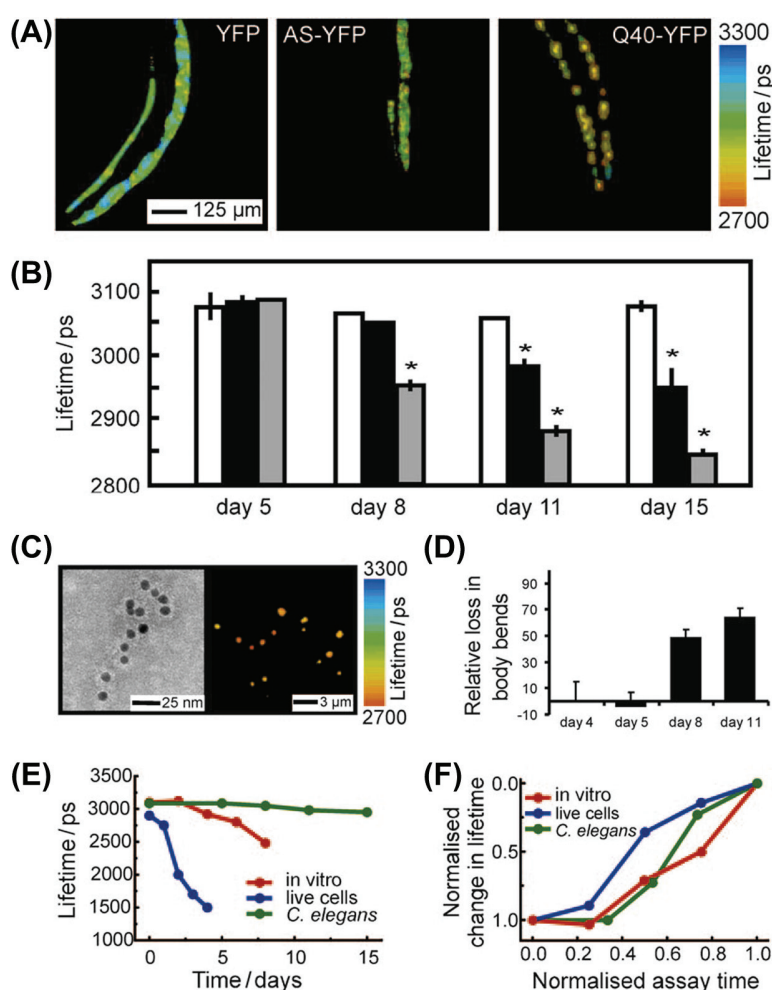
FIGURE 10.6 TCSPC lifetime imaging distinguishes the nature and kinetics of the aggregation of amyloidogenic YFP fusion protein variants during ageing in a living animal. (A) *Left*. TCSPC image of YFP transgenic *Caenorhabditis elegans* at day 11. *Center*. TCSPC image of AS–YFP transgenic *C. elegans* at day 11. *Right*. TCSPC image of Q40-YFP transgenic *C. elegans* at day 11. Note how the fluorescent aggregates display a strong reduction in the fluorescence lifetime (red color) with time. (B) Mean fluorescence lifetimes of the whole anterior part of transgenic worms expressing YFP (white), AS–YFP (black), and Q40-YFP (gray) during aging of the animals, determined at various days during the assay (mean lifetime ±SEM, ANOVA with Scheffes' post hoc test, $p < 0.05$). (C) *Ex situ* studies of *in vivo* aggregated AS–YFP. *Left*. Anti-AS immunogold-labeled TEM image of cell extracts from aged AS–YFP transgenic *C. elegans* (day 15). Only pre-fibrillar aggregates of AS–YFP are observed in these samples. *Right*. TCSPC image corresponding to the same sample as that shown on the right. (D) AS–YFP-dependent toxicity during aging in *C. elegans*. The plot shows the ratio (%) of number of bends/minute for the AS–YFP transgene versus the YFP only transgene. Because of the selective expression of the transgene in muscle cells, the toxicity phenotype is a perturbation of the motility of the worm and the toxicity readout is a reduction in the number of bends per minute. (E) Time-dependence of the decrease of fluorescence lifetime for AS–YFP in the three systems studied herein (*in vitro*, red; living SH-SY5Y cells, blue; living *C. elegans*, green). (F) Normalized kinetics of AS–YFP aggregation *in vitro* and *in vivo* determined by the decrease in fluorescence lifetime. The color code is the same as in (E). With permission from reference 9.

observed for control animals containing a YFP only transgene, but which were devoid of protein aggregates (Fig. 10.6A, first image of panel, and Fig. 10.6B, white bars). We also performed control experiments using Q40-YFP, a 40-residue polyglutamine sequence (Q40) attached to YFP, *C.elegans*. The Q40-YFP construct showed a particularly large change in the mean fluorescence lifetime as a function of time, with the system displaying a shift of around 260 ps by the end of the assay (Fig. 10.6A, third image of panel, and Fig. 10.6B, grey bars), a result attributable to the much greater rate of aggregation of Q40 relative to AS *in vitro*. We further isolated the aggregated AS–YFP species from the worms at different time points and subjected them to parallel TCSPC and immuno-TEM analysis. This analysis revealed the presence of AS immuno-positive, non-fibrillar aggregates with lifetimes of around 2700 ps (Fig. 10.6C). This value was close to that observed for pre-fibrillar species observed *in vitro*, indicating that the aggregates formed in the *C. elegans* muscle tissue are less ordered species than more mature amyloid fibrils observed *in vitro* and in mammalian neurons. The power of the method thus lies in its capability to offer clues as to the nature of aggregate species within an organism in addition to a simple verification of their presence. This has great promise to advance our understanding of disease: Because the worms are alive, the appearance of certain amyloid species can be directly correlated with toxic phenotypes: in the worms, the observed decreases in fluorescence lifetime correlates strongly with a reduction in the number of body bends performed by the AS–YFP-expressing worms compared to control animals expressing YFP only (Fig. 10.6D). This phenotype (loss of body bends) is associated with cellular damage, and thus the study strongly supports the view that pre-fibrillar rather than mature fibril species are the most toxic species in AS-mediated neurodegenerative disorders.

The sensor concept is applicable in a large range of environments, e.g. under laboratory conditions, in cells in culture, and in live animals (Fig. 10.6, E and F).

SUPER-RESOLUTION IMAGING OF AMYLOID AGGREGATION

Single-Molecule-Based Localization Microscopy for Direct Visualization of Amyloid Morphology

In order to monitor directly structural differences in amyloid aggregates at subcellular resolution, one requires refined methods that are applicable to *in situ* studies in biological systems. Label-free imaging methods, such as positron-emission tomography, optical coherence tomography, and magnetic resonance imaging, provide powerful methods for cellular imaging, but, unfortunately, do not permit the resolution of subcellular structures. On the other hand, electron microscopy (EM) and atomic force microscopy (AFM) can

be used in tissue or *in vitro* but they are not easily compatible with whole-cell imaging. Light microscopy does not suffer that latter disadvantage but it does not traditionally offer a spatial resolution that is good enough to offer molecular-level structural details. However, fluorescence spectroscopy is extremely powerful for functional microscopy through the availability of highly specific labels and a large dynamic range to probe spatial and temporal details that give insights into cellular structure and organization, even in living cells.

The spatial resolution limit, however, prevents resolution of structural features that are smaller than approximately half a wavelength of light. This obstacle has triggered the development of methods to bypass the so-called diffraction barrier, a fundamental principle in optics that was first described by Ernst Abbe in 1873 and further discussed by Rayleigh and others. After the introduction of the first concept for fluorescence imaging beyond the resolution limit [40–42] several methods have emerged that enable super-resolution imaging with optical resolution approaching the molecular scale [43–48]. Among them are stimulated emission depletion (STED), which makes use of a nonlinear saturation process for the controlled de-excitation of fluorophores [42,43] and structured illumination microscopy (SIM) [49,50], where a finely structured excitation pattern is used to demodulate high spatial frequencies that encode structural information beyond the diffraction limit. In parallel, alternative super-resolution imaging methods emerged that use precise determination of position (localization) of individual fluorophores by recording and computationally fitting their diffraction patterns in the imaging plane. Ultimately, temporal separation of fluorophore emission [51] paved the way for single-molecule-based localization microscopy by stochastic photoswitching as in photoactivated localization microscopy (PALM) [52], fluorescence photoactivation localization microscopy (FPALM) [53], stochastic optical reconstruction microscopy (STORM) [54], direct stochastic optical reconstruction microscopy (*d*STORM) [55], spectral precision distance microscopy (SPDM) [56], ground state depletion microscopy followed by individual molecule return (GSDIM) [57], blink microscopy [58], super-resolution optical fluctuation imaging (SOFI) [59], and related methods [60].

Fluorescence detection with a high signal-to-background ratio is the key for precise localization of the emission pattern of individual molecules. For negligible background noise the precision of localization depends only on the number of collected photons N and on the standard deviation of the true PSF (σ) and can be approximated by $\sigma/\sqrt{N}$ [61–63]. Given the fact that it is possible to detect thousands of fluorescence photons from a single organic fluorophore before it photobleaches, localization of individual fluorophores with one nanometer accuracy (FIONA) is feasible and was used successfully, e.g. to monitor molecular motor dynamics [64]. To achieve super-resolution fluorescence imaging, the fluorophore emission from proximate fluorophores has to be

temporally separated. In single-molecule-based localization microscopy methods this is achieved by stochastic activation of individual fluorophores, single-molecule detection using a wide-field fluorescence microscope equipped with a sensitive CCD camera, and precise position determination (localization), i.e. fitting of ideal PSFs (point spread functions) to the measured photon distributions. As long as the distance between individual fluorophores is greater than the distance resolved by the microscope in any one recorded image (> λ/2 on the CCD camera), the standard error of the fitted position can be made arbitrarily small by collecting more photons and minimizing noise factors [61,62].

The principle procedure for single-molecule-based localization microscopy is shown in Figure 10.7. A target structure is densely labeled with photoswitchable or photoactivatable fluorophores, the majority of which have to be transferred to the non-fluorescent state. During the actual experiment, only a subset of single emitters is switched on stochastically per image (see Video 1). At any point in time the density of activated fluorophores should be low enough to allow the isolated localization of individual fluorophores. Activation and localization are repeated many times, and a final image with superior resolution is reconstructed from all single-molecule positions determined.
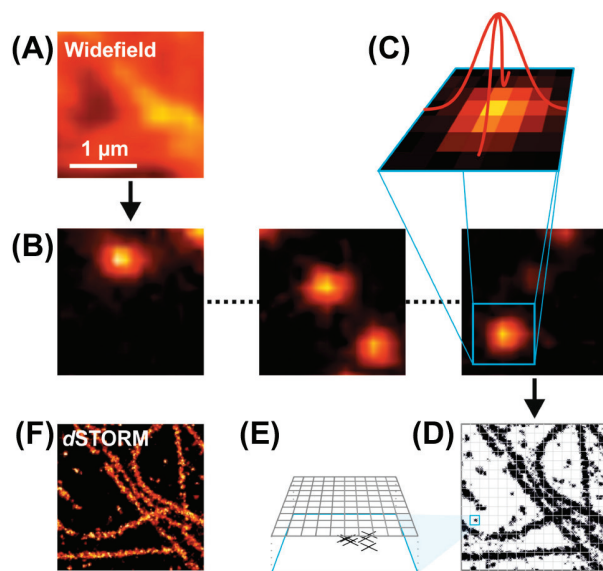
Fluorophores for Localization Microscopy

Common to all single-molecule-based localization microscopy methods is the need for fluorophores that can be photoactivated or reversibly photoswitched by irradiation with light. Such fluorophores exhibit a fluorescent on-state, a non-fluorescent off-state, and a transition between these states. The most prominent variants are photoactivatable or photoconvertible fluorescent proteins (PA-FPs) [65,66], as used in PALM and FPALM or standard organic fluorophores [67,68] or pairs of organic fluorophores, i.e. combinations of activator and reporter fluorophores [54] as used in *d*STORM and STORM. PA-FPs are genetically fused to target proteins and endogenously expressed in cells and organelles. Moreover, stable cell lines can be prepared that achieve protein labeling efficiencies approaching 100%, a level impossible to achieve by chemical staining with synthetic fluorophores. Furthermore, fluorescent proteins are smaller (a barrel with dimensions 2.4 × 4.2 nm) than e.g. fluorophore-labeled antibodies typically used in *d*STORM and STORM applications (the size of an IgG antibody is about 7–8 nm). Therefore, the density of fluorophores tagging a structure is generally lower compared to endogenously expressed PA-FPs.

Whereas the smallest resolvable distance between two fluorophores determines the optical resolution, the structural interpretation of localization microscopy data is determined by the labeling density. According to information theory, the required density of fluorescent probes for super-resolution imaging has to be sufficiently high to satisfy the

Nyquist–Shannon sampling theorem [63]. In essence, this states that the mean distance between neighboring localized fluorophores (the sampling interval) must be at least twice as fine as the desired resolution. For example, to resolve 20 nm structural features in one dimension, a fluorophore has to be localized at least every 10 nm. Extended to a two-dimensional structure, this corresponds to a labeling density of about 10^4 fluorophores μm^{-2} and translates to 600 fluorophores present within a diffraction-limited area of diameter ~250 nm. Only one of these 600 fluorophores should reside in its fluorescent state at any time of the experiment, implying that the lifetime of the off-state has to be at least 600 times longer than the lifetime of the fluorescent on-state [69].

On the other hand, PA-FPs typically exhibit a lower photostability and brightness than standard organic fluorophores. The number of detectable photons of PA-FPs is typically a few hundred photons before they bleach, whereas synthetic fluorophores can emit more than 1000 photons per cycle [70], which has a direct consequence on localization precision [61,62]. From this point of view *d*STORM and other methods employing small organic fluorophores are advantageous because the fluorophores survive under moderate excitation conditions for longer time periods (i.e. they exhibit a higher photostability), emit thousands of photons, and their photoswitching rates can be controlled by

FIGURE 10.7 Principle of single-molecule-based localization microscopy. (A) A structure is labeled with photoswitchable or photoactivatable fluorescent probes and imaged by wide-field fluorescence microscopy. Activation of only a subset of fluorophores at any time of the experiments allows the isolated detection (B) and position determination of individual fluorescent probes with high precision (C). (D) Localization pattern of all localizations performed. To improve visualization of the localization pattern, artificial subpixels with a size of ~1/10 of the regular pixel size are usually applied to color code the density of localizations (E,F). With permission from reference 45.

ONLINE VIDEO 1 (Actin-*d*Storm.avi).

external means [55,67,71]. Furthermore, a large number of commercially available fluorescent probes spanning the entire visible spectral range [67,71] can be directly used as photoswitches in aqueous solvents simply by adding millimolar concentrations of reducing thiols (Fig. 10.8). Therefore, *d*STORM has been used successfully to study the number, distribution, and density of cellular or membrane proteins in fixed cells [71–75] and the *in vitro* dynamics of molecular motor proteins [76]. Appropriate reducing conditions inside a living cell (all cells contain reducing agents such as glutathione) enable live-cell *d*STORM [77], which has been used to study the distribution and dynamics of core histone proteins [78–80] applying real-time data analysis. This opens the potential to combine *d*STORM with (F)PALM to perform multicolor super-resolution imaging experiments in living cells, profiting from orthogonal labeling strategies [81].

Realization of *Direct* Stochastic Optical Reconstruction Microscopy Experiments

In order to determine the position of single fluorophores, the fluorescence signal (given by the number of fluorescence photons detected) should be very high, whereas the background (background fluorescence and detector noise) should be as low as possible. Optimal results can be achieved by single-molecule fluorescence imaging with a high signal-to-background ratio using an inverted fluorescence microscope equipped with an oil-immersion objective with high numerical aperture (NA ≥1.45) operated in objective-type total internal reflection fluorescence (TIRF) microscopy mode. TIRF microscopy limits fluorophore excitation to a thin evanescent field (100 to 200 nm) and minimizes background light. 3D or whole-cell imaging can be realized using a wide-field configuration, at the expense of a lower signal-to-background ratio and a lower precision in single-molecule localization. An interesting approach is the illumination by a highly inclined and thin beam that allows axial sectioning (HILO) [82]. For excitation, either a multi-line argon–krypton gas-ion laser in combination with a 405 nm diode laser or single-line semiconductor lasers emitting at 405, 488, 532, 568, 640, and 660 nm, with an output power of 100 mW, should be used. Laser lines are combined by suitable dichroic mirrors and/or selected by an acousto-optical tunable filter (AOTF) and coupled into the microscope objective using an appropriate polychromatic mirror. Typically, excitation intensities in the range of 1–5 kW cm^{-2} have to be applied for readout and photoswitching at frame rates of 10–100 Hz. For recovery of the on-state, excitation intensities at 405 nm – well below 1 kW cm^{-2} (e.g. 0–0.1 kW cm^{-2}) [83] – are sufficient.
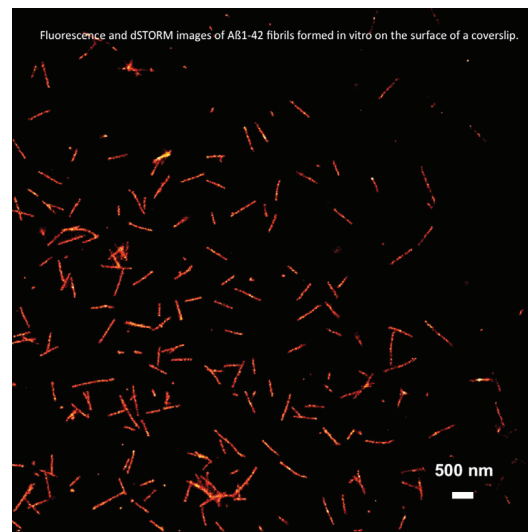
The fluorescence light in the detection path is filtered using suitable bandpass filters and imaged with an electron-multiplying CCD camera. The CCD chip collects the incoming photons in pixels with a typical size in the range of 16 × 16 μm^2 to 24 × 24 μm^2. To preserve most of the position information in the fluorescence signal data, a pixel size of ~ 2.3× smaller than the Abbe resolution limit of the optical system is generally used. Thus, for visible light, the fluorescence signal should be imaged ensuring a pixel size of 80–160 nm (typically ~100 nm) using appropriate additional lenses. Finally, a video sequence containing several thousands of images is recorded.
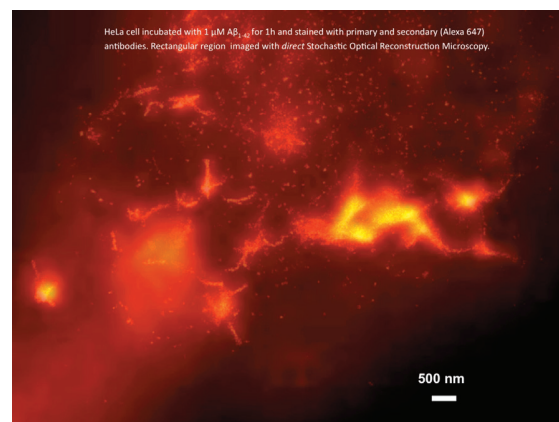
In Situ Imaging of Abeta 40 and Abeta 42 Self Assembly Reactions

To demonstrate the capability of *d*STORM in the study of protein aggregation, Aß$_{1-42}$ amyloid fibrils were formed *in vitro* by diluting the monomeric peptide in 50 mM sodium phosphate buffer, pH 7.4, and incubating it at room temperature for 4 days prior to examination by transmission electron microscopy (TEM) and super-resolution imaging. Cells were plated on LabTek II 8-well chambered coverglass. For detailed information see reference 8. After 12–24 hours, the medium was replaced with medium without FCS and the cells were incubated either with HiLyte Fluor™ 647 cys-Aß$_{1-40}$ or with unlabeled Aß$_{1-42}$ for 1 hour prior to fixation. Unlabeled Aβ$_{1-42}$ was stained by indirect immunochemistry using monoclonal anti-Aß antibody and Alexa Fluor® 647 goat anti-mouse IgG antibody, respectively. In both cases we typically detected 1000–5000 photons per frame from single fluorophores, allowing a localization precision of better than 20 nm in the imaging plane, experimentally determined from repetitive localizations of individual Alexa Fluor® 647 labeled antibodies (see Video 2). For TEM experiments Aß$_{1-42}$ was adsorbed onto formvarcoated 400 Mesh copper grids for 5–10 minutes and negatively stained with 2% (w/v) uranyl acetate (Fig. 10.9).
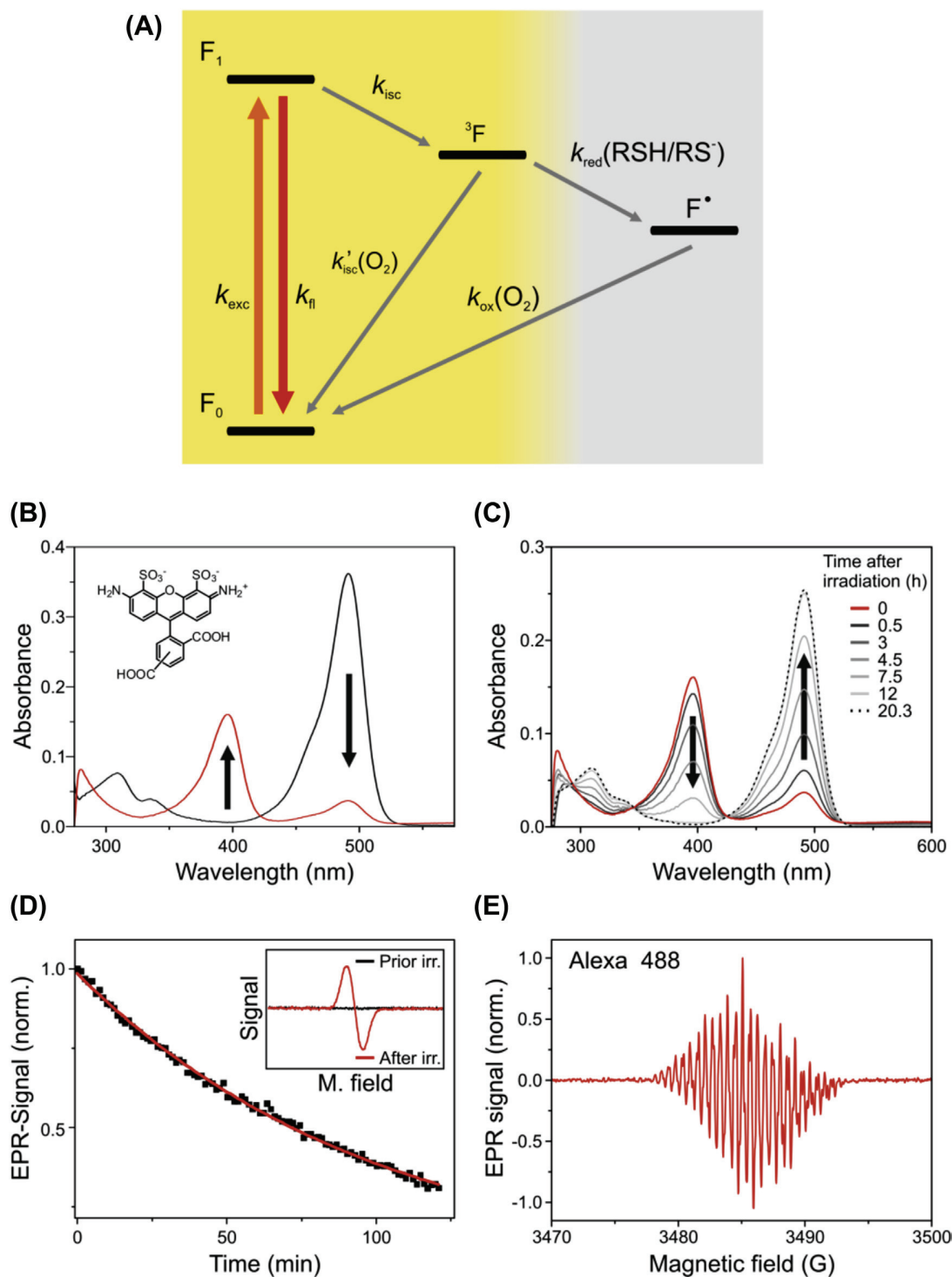
Direct comparison of the images shown in Figure 10.9 demonstrates that *d*STORM achieves a resolution approaching that of EM techniques. These images were obtained in total internal reflection fluorescence (TIRF) mode to image fibrils immobilized on the sample coverslip. To unravel the morphology of fibrils and other important details of intracellular aggregate formation of Aß$_{1-40}$ and Aß$_{1-42}$ deep inside of cells when exogenously added to cells in culture, we performed additional *d*STORM experiments. Whereas cells in contact with soluble Aß$_{1-40}$ showed, at most, only small oligomeric species within cells (Fig. 10.10), cells treated with a 1 μM solution of Aß$_{1-42}$ unequivocally unravel the morphology of the fibrillar structures (see Video 3). Figure 10.10 underscores the resolution improvement attained by *d*STORM compared to conventional TIRF microscopy. *d*STORM can easily resolve adjacent fibrils well below the diffraction limit. Fibril diameters were determined to be in the 40–50 nm range from the full width half-maximum points of cross-sectional profiles. In addition to the actual fibril diameter, there is a significant contribution to this width from the size of the fluorescent antibodies used in the immunochemical labeling procedure.

Fluorescence and dSTORM images of Aß1-42 fibrils formed in vitro on the surface of a coverslip.

500 nm

ONLINE VIDEO 2 (Abeta42_dStorm_in vitro.mpg).

HeLa cell incubated with 1 µM Aβ₁₋₄₂ for 1h and stained with primary and secondary (Alexa 647) antibodies. Rectangular region imaged with *direct* Stochastic Optical Reconstruction Microscopy.

500 nm

ONLINE VIDEO 3 (Abeta42_dSTORM_HeLa.mpg).

FIGURE 10.8   Reaction scheme, absorption, and EPR spectra of stable rhodamine radicals. (A) The dye is excited with rate k_{exc}, fluoresces with k_{fl}, or enters the triplet state (^{3}F) dependent on its intersystem crossing rate k_{isc}. The triplet state of the fluorophore can react with oxygen ($k'_{isc}(O_2)$) to repopulate the singlet ground state F_0 and produce singlet oxygen $^1O_2$, or react with the thiol with rate $k_{red}(RSH/RS-)$ to form the semi-reduced dye radical ($F^{\bullet}$) and the thiyl radical ($RS^{\bullet}$). The semireduced dye radical can react with oxygen to repopulate the fluorescent singlet state with rate $k_{ox}(O_2)$. (B) Absorption spectra of an aqueous Alexa Fluor 488 solution containing 100 mM MEA, pH 9.3 before and after irradiation at 488 nm for 5 min. The radical anion exhibits an absorption maximum at 396 nm with an extinction coefficient of $\varepsilon = 5.1 \times 10^4 \, l \, mol^{-1} \, cm^{-1}$. (C) Absorption spectra of Alexa Fluor 488 measured in a sealed cuvette with time after photoreduction. The lifetime of the radical anion was determined to be about 7 hours. (D,E) EPR spectra and time-dependent behavior of the signal of a 10^{-4} M aqueous solution of Alexa Fluor 488 in the presence of 100 mM MEA, pH 9.3 after irradiation at 488 nm for several minutes. The exponential decay of the EPR signal reveals a radical lifetime of ~100 minutes in non-sealed EPR capillary tubes. The pH of the solution was increased to 9.3 to facilitate photoreduction. The radical anion disappears immediately upon purging of the capillary with air. With permission from reference 83.
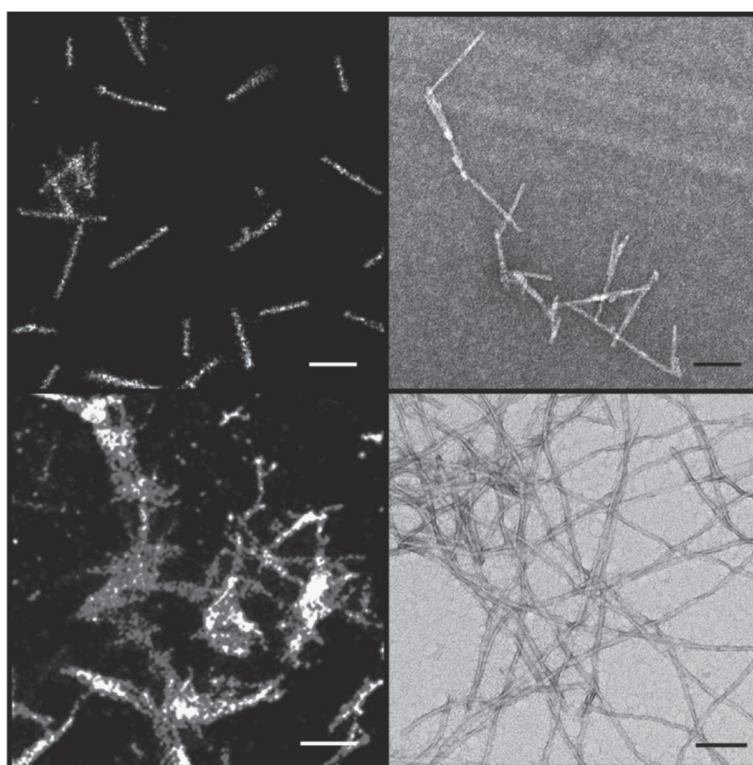
FIGURE 10.9   Top row. *Left*. *d*STORM image of extracellular Aβ$_{1-42}$ aggregates with which cells were incubated. *Right*. Corresponding TEM image of *in vitro* Aβ$_{1-42}$ aggregates. Bottom row. *Left*. *d*STORM image of a section of a cell containing Aβ$_{1-42}$ fibrils. *Right*. TEM image of Aβ$_{1-42}$ fibrils formed *in vitro* after 4 days at room temperature. White scale bars: 500 nm; black scale bars: 100 nm. With permission from reference 8.

The *d*STORM images were subjected to more detailed analysis in order to probe the morphology of the intracellular aggregates of Aβ. Cross sections of the fibrils show (Fig. 10.10) that the lateral resolution achieved by *d*STORM is sufficient to identify individual fibrils both *in vitro* and *in vivo* and reveal that intracellular fibrils have a similar morphology to that of fibrils observed *in vitro*. In particular, intracellular fibrils show a multimodal distribution of lengths in the range 0.3 to 1.9 μm [8]. The majority appear straight, but about 10% of the fibrils exhibit bending angles in the range 135°–165° [8]. These characteristics are similar to those observed for Aβ$_{1-42}$ fibrils derived from the postmortem brains of AD patients [84].

Super-Resolution Imaging of Human Lysozyme

In a different example to probe amyloidogenesis *via* super-resolution imaging, we examined the formation of fibrils from mutational variants of human lysozyme, which is associated with a fatal form of hereditary non-neuropathic systemic amyloidosis. Super-resolution imaging has potential to unravel mechanistic details of lysozyme aggregation and help to further our knowledge of misfolding conditions and their relation to disease progression [85]. We have recently shown that a biotin moiety can be introduced at the

Lys33 site of human lysozyme such that both the protein's native state and its aggregation kinetics are not measurably altered. This then permits the introduction of labels suitable for *d*STORM super-resolution imaging through the use of biotin–avidin interactions. The *d*STORM analysis of the biotin–human lysozyme aggregates clearly reveals fluorescent fibrils with greatly improved resolution compared to that achievable with conventional fluorescence techniques (Fig. 10.11, A–F). Figure 10.11D shows a fibril bundle with a diameter of 133±20 nm, which is comparable to the diameter observed in the TEM images of similar bundles (approximately 100–200 nm) (Fig. 10.11G). For further details please see reference 85.

CONCLUSION

In this chapter we have reviewed novel fluorescence imaging techniques capable of following protein aggregation kinetics in real time, both *in vitro* and *in vivo*. With indirect techniques such as homoFRET and fluorescence lifetime imaging it is possible to glean information on the aggregation state dynamically in complex model systems of disease. Examples include the study of toxic phenotypes in animal models, which can be correlated to the degree of aggregation of amyloidogenic species. We also describe an optical super-resolution method, with which it is possible to obtain
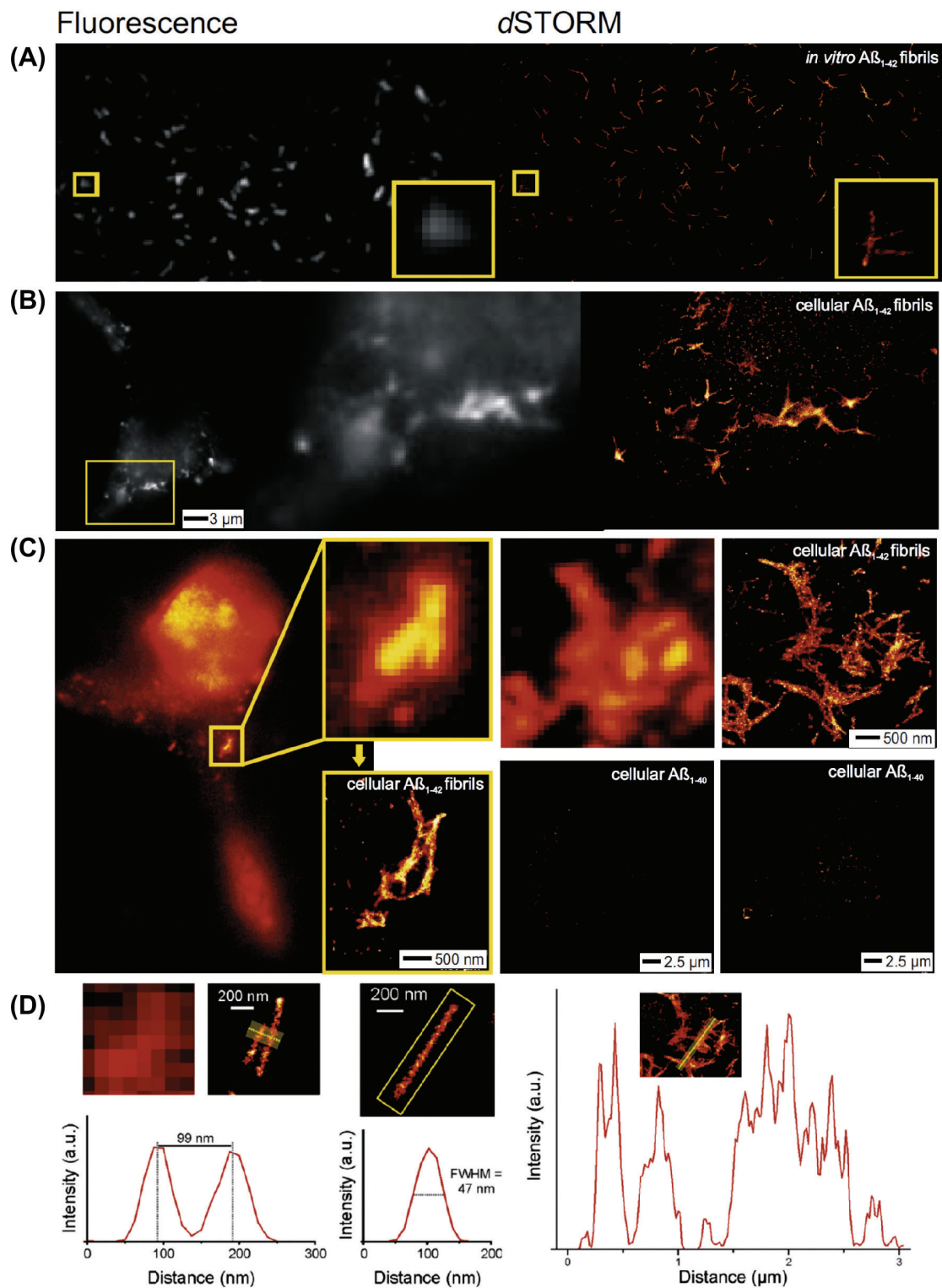
FIGURE 10.10 (A) *d*STORM image of extracellular Aβ$_{1-42}$ aggregates. (B,C) Fluorescence and corresponding *d*STORM images showing small oligo-meric and fibrillar forms of Aβ$_{1-40}$ and Aβ$_{1-42}$ formed within HeLa cells detected with a primary antibody against Aβ and a secondary antibody conjugated with Alexa Fluor 647. (D) Adjacent fibrils can be resolved well below the diffraction limit. Fibril diameters were determined to be in the 40–50 nm range from the full width half-maximum points of cross-sectional profiles. Intensity profile across a transverse section of a *d*STORM image displaying intracel-lular Aβ$_{1-42}$ aggregates. Yellow rectangles on the panels indicate the same field of view. Images were recorded in highly inclined illumination mode [85]. With permission from reference 8.
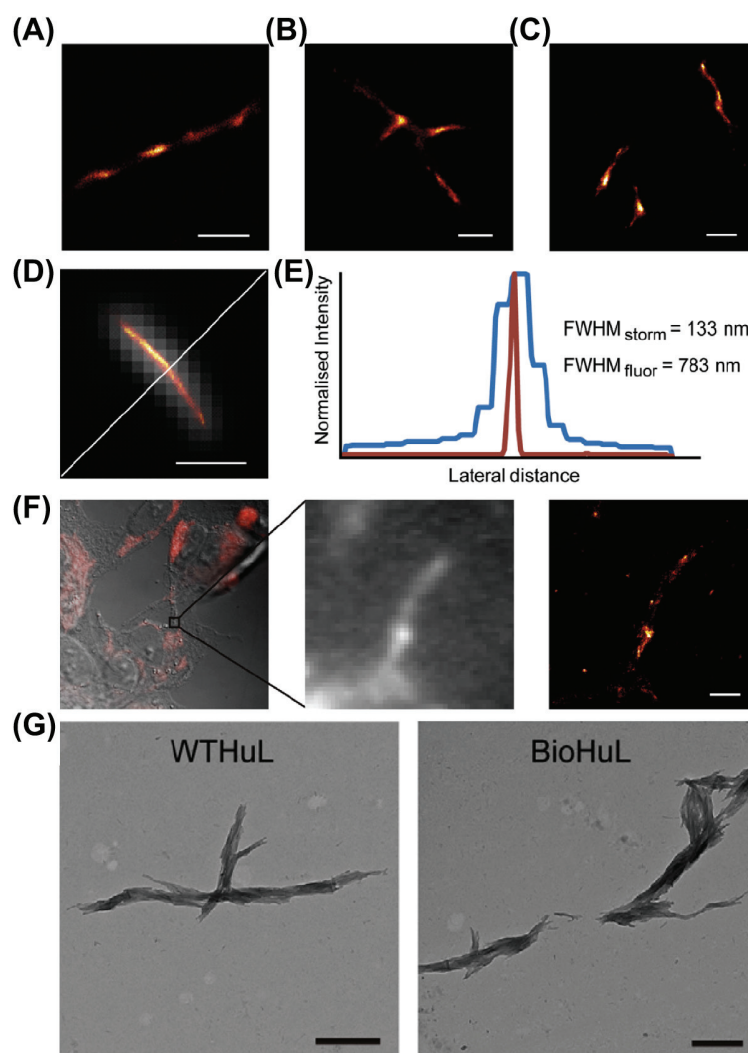
FIGURE 10.11 (A–C) Super-resolution *d*STORM images of different biotin–human lysozyme (BioHuL) fibrils (formed *in vitro*). (D) An overlay of a straight BioHuL fibril with its fluorescence sum image. (E) The cross-sections of the individual fluorescence sum and the super-resolved *d*STORM image of the BioHuL fibril displayed in panel (D). The full-width half-maximum (FWHM) of the fluorescence intensity distribution of the unresolved sum image depicts a fibril diameter of 783 nm whereas the super-resolved image depicts a fibril diameter of 133 nm; the latter showing 6 times better resolution. (F) *Left panel*. DIC image of BioHuL present within SH-SY5Y mammalian cells after probing with streptavidin-Alexa647. *Center panel*. Fluorescence sum image of a region within the SH-SY5Y cells. *Right panel*. Super-resolution *d*STORM images of BioHuL fibrils in the same region of the SH-SY5Y mammalian cells as the fluorescence sum image. All scale bars represent 1 μm. (G) TEM images on the left and right show the fibrils formed by WTHuL and BioHuL, respectively; the scale bars represent 500 nm. BioHuL (gray) and WTHuL (black) were incubated in the presence of 3 M urea in 0.1 M citrate buffer (pH 5.0) with constant stirring at 60°C. With permission from reference 85.

images of amyloid structure at a resolution approaching that of electron microscopy techniques, but which retains the advantages of fluorescence techniques and thus is capable of application in cells and organisms. These very recent developments are set to change our capability to study molecular mechanisms of aggregation diseases

ACKNOWLEDGMENTS

REFERENCES

[1] Dobson CM. Protein folding and misfolding. Nature 2003;426(6968):884–90.

[2] Selkoe DJ. Cell biology of protein misfolding: the examples of Alzheimer's and Parkinson's diseases. Nature Cell Biol 2004;6(11):1054–61.

[3] Meyer-Luehmann M, Spires-Jones TL, Prada C, Garcia-Alloza M, de Calignon A, Rozkalne A, et al. Rapid appearance and local toxicity of amyloid-beta plaques in a mouse model of Alzheimer's disease. Nature 2008;451(7179):720–4.

[4] Caughey B, Lansbury PT. Protofibrils, pores, fibrils, and neurodegeneration: separating the responsible protein aggregates from the innocent bystanders. Annu Rev Neurosci 2003;26:267–98.

[5] Bacskai BJ, Hickey GA, Skoch J, Kajdasz ST, Wang Y, Huang G-F, et al. Four-dimensional multiphoton imaging of brain entry, amyloid binding, and clearance of an amyloid-beta ligand in transgenic mice. Proc Natl Acad Sci USA 2003;100(21):12462–7.

[6] Roberti MJ, Bertoncini CW, Klement R, Jares-Erijman EA, Jovin TM. Fluorescence imaging of amyloid formation in living cells by a functional, tetracysteine-tagged alpha-synuclein. Nature Meth 2007;4(4):345–51.

[7] Bacskai BJ, Skoch J, Hickey GA, Allen R, Hyman BT. Fluorescence resonance energy transfer determinations using multiphoton fluorescence lifetime imaging microscopy to characterize amyloid-beta plaques. J Biomed Optics 2003;8(3):368–75.

[8] Kaminski Schierle GS, van de Linde S, Erdelyi M, Esbjörner EK, Klein T, Rees E, et al. *In Situ* measurements of the formation and morphology of intracellular ß-amyloid fibrils by super-resolution fluorescence imaging. Journal of the Am Chem Soc 2011;133(33):12902–5.

[9] Kaminski Schierle GS, Bertoncini CW, Chan FTS, Van der Goot AT, Schwedler S, Skepper J, et al. A FRET sensor for non-invasive imaging of amyloid formation *in vivo*. ChemPhyschem 2011;12(3):673–80.

[10] Roberti MJ, Fölling J, Celej MS, Bossi M, Jovin TM, Jares-Erijman E. Imaging nanometer-sized α-synuclein aggregates by superresolution fluorescence localization microscopy. Biophys J 2012;102(7): 1598–607.

[11] Dai X, Eccleston ME, Yue Z, Slater NKH, Kaminski CF. A spectroscopic study of the self-association and inter-molecular aggregation behaviour of pH-responsive poly (L -lysine iso-phthalamide). Polymer 2006;47:2689–98.

[12] Frank JH, Elder AD, Swartling J, Venkitaraman AR, Jeyasekharan AD, Kaminski CF. A white light confocal microscope for spectrally resolved multidimensional imaging. J Microsc 2007;227:203–15.

[13] Schlachter S, Schwedler S, Esposito A, Kaminski Schierle GS, Moggridge GD, Kaminski CF. A method to unmix multiple fluorophores in microscopy images with minimal a priori information. Optics Express 2009;17(25):22747–60.

[14] Van Ham TJ, Thijssen KL, Breitling R, Hofstra RMW, Plasterk RHA, Nollen EAA. *C. elegans* model identifies genetic modifiers of alpha-synuclein inclusion formation during aging. PLoS Genet 2008;4(3):e1000027.

[15] Rockenstein E, Schwach G, Ingolic E, Adame A, Crews L, Mante M, et al. Lysosomal pathology associated with alpha-synuclein accumulation in transgenic models using an eGFP fusion protein. J Neurosci Res 2005;80(2):247–59.

[16] Muchowski PJ, Ramsden R, Nguyen Q, Arnett EE, Greiling TM, Anderson SK, et al. Noninvasive measurement of protein aggregation by mutant huntingtin fragments or alpha-synuclein in the lens. J Biol Chem 2008;283(10):6330–6.

[17] Cooper AA, Gitler AD, Cashikar A, Haynes CM, Hill KJ, Bhullar B, et al. Alpha-synuclein blocks ER-Golgi traffic and Rab1 rescues neuron loss in Parkinson's models. Science 2006;313(5785): 324–8.

[18] Wang J, Farr GW, Hall DH, Li F, Furtak K, Dreier L, et al. An ALS-linked mutant SOD1 produces a locomotor defect associated with aggregation and synaptic dysfunction when expressed in neurons of Caenorhabditis elegans. PLoS Genet 2009;5(1):e1000350.

[19] Nollen EAA, Garcia SM, Van Haaften G, Kim S, Chavez A, Morimoto RI, et al. Genome-wide RNA interference screen identifies previously undescribed regulators of polyglutamine aggregation. Proc Natl Acad Sci USA 2004;101(17):6403–8.

[20] Satyal SH, Schmidt E, Kitagawa K, Sondheimer N, Lindquist S, Kramer JM, et al. Polyglutamine aggregates alter protein folding homeostasis in *Caenorhabditis elegans*. Proc Natl Acad Sci USA 2000;97(11):5750–5.

[21] Hamada D, Tsumoto K, Sawara M, Tanaka N, Nakahira K, Shiraki K, et al. Effect of an amyloidogenic sequence attached to yellow fluorescent protein. Proteins 2008;72(3):811–21.

[22] Murakami T, Yang S-P, Xie L, Kawano T, Fu D, Mukai A, et al. Kaminski Schierle GS, Chan FTS, Moloney A, Crowther D, Kaminski CF, Zhen M, St George-Hyslop P. ALS mutations in FUS cause neuronal dysfunction and death in *Caenorhabditis elegans* by a dominant gain-of-function mechanism. Hum Mol Genet 2012;21(1):1–9.

[23] Van Ham TJ, Esposito A, Kumita JR, Hsu S-TD, Kaminski Schierle GS, Kaminski CF, et al. Towards multiparametric fluorescent imaging of amyloid formation: studies of a YFP model of alpha-synuclein aggregation. J Mol Biol 2010;395(3):627–42.

[24] Fernández CO, Hoyer W, Zweckstetter M, Jares-Erijman EA, Subramaniam V, Griesinger C, et al. NMR of alpha-synuclein-polyamine complexes elucidates the mechanism and kinetics of induced aggregation. EMBO J 2004;23(10):2039–46.

[25] Croke RL, Sallum CO, Watson E, Watt ED, Alexandrescu AT. Hydrogen exchange of monomeric alpha-synuclein shows unfolded structure persists at physiological temperature and is independent of molecular crowding in *Escherichia coli*. Protein Sci 2008;17(8):1434–45.

[26] Hsu S-TD, Bertoncini CW, Dobson CM. Use of protonless NMR spectroscopy to alleviate the loss of information resulting from exchange-broadening. J Am Chem Soc 2009;131(21):7222–3.

[27] Schlachter S, Elder A, Frank JH, Grudinin A, Kaminski CF. Spectrally resolved confocal fluorescence microscopy with a supercontinuum laser. Microsc Analysis 2008;22(3):11–3.

[28] Esposito A, Bader AN, Schlachter SC, Van Den Heuvel DJ, Kaminski Schierle GS, Venkitaraman AR, et al. Design and application of a confocal microscope for spectrally resolved anisotropy imaging. Optics Express 2011;19(3):2546–55.

[29] Elder AD, Matthews SM, Swartling J, Yunus K, Frank JH, Brennan CM, et al. Application of frequency-domain fluorescence lifetime imaging microscopy as a quantitative analytical tool for microfluidic devices. Optics Express 2006;14(12):5456–67.

[30] Jares-Erijman EA, Jovin TM. FRET imaging. Nature Biotechnol 2003;21(11):1387–95.

[31] Elder AD, Domin A, Kaminski Schierle GS, Lindon C, Pines J, Esposito A, et al. A quantitative protocol for dynamic measurements of protein interactions by FRET-sensitized fluorescence emission. J R Soc Interface 2009;6:59–81.

[32] Chan FTS, Kaminski CF. Kaminski Schierle GS. HomoFRET fluorescence anisotropy imaging as a tool to study molecular self-assembly in live cells. ChemPhysChem 2011;12(3):500–9.

[33] Elder AD, Frank JH, Swartling J, Dai X, Kaminski CF. Calibration of a wide-field frequency-domain fluorescence lifetime microscopy system using light emitting diodes as light sources. J Microsc 2006;224(Pt 2):166–80.

[34] Elder AD, Kaminski CF, Frank JH. phi(FLIM)-F-2: a technique for alias-free frequency domain fluorescence lifetime imaging. Optics Express 2009;17(25):23181–203.

[35] Chan FTS, Kaminski Schierle GS, Kumita JR, Bertoncini CW, Dobson CM, Kaminski CF. Protein amyloids develop an intrinsic fluorescence signature during aggregation. Analyst 2013;138(7):2156–62.

[36] Pinotsi D, Buell AK, Dobson CM. Kaminski Schierle GS, Kaminski CF. A label-free, quantitative assay of amyloid fibril growth based on intrinsic fluorescence. ChemBioChem 2013. http://dx.doi.org/10.1002/cbic.201300103.

[37] Del Mercato LL, Pompa PP, Maruccio G, Della Torre A, Sabella S, Tamburro AM, et al. Charge transport and intrinsic fluorescence in amyloid-like fibrils. Proc Natl Acad Sci USA 2007;104(46):18019–24.

[38] Shukla A, Mukherjee S, Sharma S, Agrawal V. Radha Kishan K V, Guptasarma P. A novel UV laser-induced visible blue radiation from protein crystals and aggregates: scattering artifacts or fluorescence transitions of peptide electrons delocalized through hydrogen bonding? Arch Biochem Biophys 2004;428(2):144–53.

[39] Sharpe S, Simonetti K, Yau J, Walsh P. Solid-State NMR characterization of autofluorescent fibrils formed by the elastin-derived peptide GVGVAGVG. Biomacromolecules 2011;12(5):1546–55.

[40] Betzig E, Trautman JK. Near-field optics: microscopy, spectroscopy, and surface modification beyond the diffraction limit. Science 1992;257(5067):189–95.

[41] Hell S, Stelzer EHK. Fundamental improvement of resolution with a 4Pi-confocal fluorescence microscope using two-photon excitation. Optics Commun 1992;93(5-6):277–82.

[42] Hell SW, Wichmann J. Breaking the diffraction resolution limit by stimulated emission: stimulated-emission-depletion fluorescence microscopy. Optics Lett 1994;19(11):780–2.

[43] Hell SW. Far-field optical nanoscopy. Science 2007;316(5828):1153–8.

[44] Galbraith CG, Galbraith JA. Super-resolution microscopy at a glance. J Cell Sci 2011;124(Pt 10):1607–11.

[45] Van de Linde S, Wolter S, Sauer M. Single-molecule photoswitching and localization. Aust J Chem 2011;64:503–11.

[46] Heilemann M, Dedecker P, Hofkens J, Sauer M. Photoswitches: key molecules for subdiffraction-resolution fluorescence imaging and molecular quantification. Laser Photonics Rev 2009;3(1-2):180–202.

[47] Ji N, Shroff H, Zhong H, Betzig E. Advances in the speed and resolution of light microscopy. Curr Opin Neurobiol 2008;18(6):605–16.

[48] Patterson G, Davidson M, Manley S, Lippincott-Schwartz J. Super-resolution imaging using single-molecule localization. Annu Rev Phys Chem 2010;61:345–67.

[49] Gustafsson MG. Surpassing the lateral resolution limit by a factor of two using structured illumination microscopy. J Microsc 2000;198(Pt 2):82–7.

[50] Kner P, Chhun BB, Griffis ER, Winoto L, Gustafsson MGL, America N. Super-resolution video microscopy of live cells by structured illumination. Nature Meth 2009;6(5):339–42.

[51] Lidke K, Rieger B, Jovin T, Heintzmann R. Superresolution by localization of quantum dots using blinking statistics. Optics Express 2005;13(18):7052–62.

[52] Betzig E, Patterson GH, Sougrat R, Lindwasser OW, Olenych S, Bonifacino JS, et al. Imaging intracellular fluorescent proteins at nanometer resolution. Science 2006;313(5793):1642–5.

[53] Hess ST, Girirajan TPK, Mason MD. Ultra-high resolution imaging by fluorescence photoactivation localization microscopy. Biophys J 2006;91(11):4258–72.

[54] Rust MJ, Bates M, Zhuang X. Sub-diffraction-limit imaging by stochastic optical reconstruction microscopy (STORM). Nature Meth 2006;3(10):793–5.

[55] Heilemann M, Van de Linde S, Schüttpelz M, Kasper R, Seefeldt B, Mukherjee A, et al. Subdiffraction-resolution fluorescence imaging with conventional fluorescent probes. Angewandte Chemie 2008; 47(33):6172–6.

[56] Lemmer P, Gunkel M, Baddeley D, Kaufmann R, Urich A, Weiland Y, et al. light microscopy with single-molecule resolution at the nanoscale. Appl Physics B 2008;93(1):1–2.

[57] Fölling J, Bossi M, Bock H, Medda R, Wurm CA, Hein B, et al. Fluorescence nanoscopy by ground-state depletion and single-molecule return. Nature Meth 2008;5(11):943–5.

[58] Steinhauer C, Forthmann C, Vogelsang J, Tinnefeld P. Superresolution microscopy on the basis of engineered dark states. J Am Chem Soc 2008;130(50):16840–1.

[59] Dertinger T, Colyer R, Iyer G, Weiss S, Enderlein J. Fast, background-free, 3D super-resolution optical fluctuation imaging (SOFI). Proc Natl Acad Sci USA 2009;106(52):22287–92.

[60] Flors C, Ravarani CNJ, Dryden DTF. Super-resolution imaging of DNA labelled with intercalating dyes. ChemPhysChem 2009;10(13):2201–4.

[61] Thompson RE, Larson DR, Webb WW. Precise nanometer localization analysis for individual fluorescent probes. Biophys J 2002;82(5):2775–83.

[62] Mortensen KI, Churchman LS, Spudich JA, Flyvbjerg H. Optimized localization analysis for single-molecule tracking and super-resolution microscopy. Nature Meth 2010;7(5):377–81.

[63] Rees EJ, Erdelyi M, Pinotsi D, Knight A, Metcalf D, Kaminski CF. Blind assessment of localisation microscope image resolution. Optical Nanosc 2012;1(1):12.

[64] Yildiz A, Forkey JN, McKinney SA, Ha T, Goldman YE, Selvin PR. Myosin V walks hand-over-hand: single fluorophore imaging with 1.5-nm localization. Science 2003;300(5628):2061–5.

[65] Gould TJ, Verkhusha VV, Hess ST. Imaging biological structures with fluorescence photoactivation localization microscopy. Nature Protocols 2009;4(3):291–308.

[66] Shroff H, White H, Betzig E. Photoactivated localization microscopy (PALM) of adhesion complexes. Curr Protocols Cell Biol 2008; Chapter 4:Unit 4.21.

[67] Van de Linde S, Löschberger A, Klein T, Heidbreder M, Wolter S, Heilemann M, et al. Direct stochastic optical reconstruction microscopy with standard fluorescent probes. Nature Protocols 2011;6(7):991–1009.

[68] Dempsey GT, Vaughan JC, Chen KH, Bates M, Zhuang X. Evaluation of fluorophores for optimal performance in localization-based super-resolution imaging. Nature Meth 2011;8(12):1027–36.

[69] Van de Linde S, Wolter S, Heilemann M, Sauer M. The effect of photoswitching kinetics and labeling densities on super-resolution fluorescence imaging. J Biotechnol 2010;149(4):260–6.

[70] Tang J, Akerboom J, Vaziri A, Looger LL, Shank CV. Near-isotropic 3D optical nanoscopy with photon-limited chromophores. Proc Natl Acad Sci USA 2010;107(22):10068–73.

[71] Heilemann M, Van de Linde S, Mukherjee A, Sauer M. Super-resolution imaging with small organic fluorophores. Angewandte Chemie 2009 Jan;48(37):6903–8.

[72] Van de Linde S, Sauer M, Heilemann M. Subdiffraction-resolution fluorescence imaging of proteins in the mitochondrial inner membrane with photoswitchable fluorophores. J Struct Biol 2008;164(3):250–4.

[73] Owen DM, Rentero C, Rossy J, Magenau A, Williamson D, Rodriguez M, et al. PALM imaging and cluster analysis of protein heterogeneity at the cell surface. J Biophoton 2010;3(7):446–54.

[74] Williamson DJ, Owen DM, Rossy J, Magenau A, Wehrmann M, Gooding JJ, et al. Pre-existing clusters of the adaptor Lat do not participate in early T cell signaling events. Nature Immunol 2011; 12(7):655–62.

[75] Bar-On D, Wolter S, Van de Linde S, Heilemann M, Nudelman G, Nachliel E, et al. Super-resolution imaging reveals the internal architecture of nano-sized syntaxin clusters. J Biol Chem 2012;287(32): 27158–67.

[76] Endesfelder U, Van de Linde S, Wolter S, Sauer M, Heilemann M. Subdiffraction-resolution fluorescence microscopy of myosin-actin motility. Chemphyschem 2010;11(4):836–40.

[77] Van de Linde S, Heilemann M, Sauer M. Live-cell super-resolution imaging with synthetic fluorophores. Annu Rev Phys Chem 2012;63:519–40.

[78] Wombacher R, Heidbreder M, Van de Linde S, Sheetz MP, Heilemann M, Cornish VW, et al. Live-cell super-resolution imaging with trimethoprim conjugates. Nature Meth 2010;7(9):717–9.

[79] Klein T, Löschberger A, Proppert S, Wolter S, Van de Linde S, Sauer M. Live-cell *d*STORM with SNAP-tag fusion proteins. Nature Meth 2011;8(1):7–9.

[80] Klein T, Van de Linde S, Sauer M. Live-cell super-resolution imaging goes multicolor. Chembiochem 2012;13(13):1861–3.

[81] Wilmes S, Staufenbiel M, Lisse D, Richter CP, Beutel O, Busch KB, et al. Triple-color super-resolution imaging of live cells: resolving submicroscopic receptor organization in the plasma membrane. Angewandte Chemie 2012;51(20):4868–71.

[82] Tokunaga M, Imamoto N, Sakata-Sogawa K. Highly inclined thin illumination enables clear single-molecule imaging in cells. Nature Meth 2008;5(2):159–61.

[83] Van de Linde S, Krstić I, Prisner T, Doose S, Heilemann M, Sauer M. Photoinduced formation of reversible dye radicals and their impact on super-resolution imaging. Photochem Photobiol Sci 2011;10(4):499–506.

[84] Paravastu AK, Qahwash I, Leapman RD, Meredith SC, Tycko R. Seeded growth of beta-amyloid fibrils from Alzheimer's brain-derived fibrils produces a distinct fibril structure. Proc Natl Acad Sci USA 2009;106(18):7443–8.

[85] Ahn M, De Genst E, Kaminski Schierle GS, Erdelyi M, Kaminski CF, Dobson CM, et al. Analysis of the native structure, stability and aggregation of biotinylated human lysozyme. PLoS One 2012;7(11):e50192.